CrossMark

# Effect of homogenization (microfluidization) process parameters in mechanical production of micro- and nanofibrillated cellulose on its rheological and morphological properties

**Hesam Taheri · Pieter Samyn**

**Abstract** The rheological properties of microfibrillated cellulose (MFC)/nanofibrillated cellulose (NFC) suspensions have an important role during processing and mixing. In this work, the process parameters for MFC/NFC production within a microfluidizer (i.e., the size of interaction chamber and number of passes) were varied to investigate the influences on morphology, zeta potential, chemical properties and rheological features including viscosity, creep, strain recovery and yield stress behavior. The stability and appropriate viscosity of the fiber suspensions can be controlled by optimizing the processing conditions, resulting in a reduction in fiber diameter and most negative zeta potential value. The viscosity increased with higher amount of fibrillation by using a smaller chamber or higher number of passes, but intermediate plateau values are characteristic for temporary aggregation and breaking-up of the fiber network. The creep response and yield stress have been described by parameters of the Burger model and Herschel–Bulkley model, respectively, showing a more prominent effect on yield stress of chamber size than number of passes. The network formation leads to lower creep compliance and step-like strain recovery. The transition from gel-like to liquid-like behavior as characterized by the dynamic yield point at a specific strain, is almost independent of the processing conditions. Most important, the total number of passes applied in production can be directly related to the rotational Péclet number, which combines rheological and morphological data.

**Keywords** Microfibrillated cellulose · Processing · Morphology · Viscosity · Creep

H. Taheri · P. Samyn (✉)
Chair for Bio-based Materials Engineering, Faculty of Environment and Natural Resources, Freiburg Institute for Advanced Studies (FRIAS), University of Freiburg, Habsburgerstrasse 49, 79104 Freiburg, Germany
e-mail: pieter.samyn@fobawi.uni-freiburg.de; pieter.samyn@outlook.be

H. Taheri · P. Samyn
Freiburg Materials Research Center, Stefan-Meier-Straße 21, 79104 Freiburg, Germany

H. Taheri
Hermann Staudinger Graduate School, University of Freiburg, Hebelstraße 27, 79104 Freiburg, Germany

## Introduction

Micro- and nanofibrillated cellulose (MFC and NFC) were first produced in 1983 (Herrick et al. 1983), by extracting fibrillated fibers from different wood pulps. Several techniques based on mechanical separation of elementary fibrils and their bundles from native cellulosic fibers have been used, such as homogenization, microfluidization, microgrinding, cryocrushing or ultrasonication. During high-pressure homogenization,

the high shear rate within a homogenizer chamber causes fibrillation of the fibers in aqueous suspension. The microfibrillated cellulose (MFC) or nanofibrillated cellulose (NFC) terms are designated for long flexible nanofibers with either micro- or nanoscale fiber diameters and high aspect ratio, consisting of crystalline and amorphous states (Moon et al. 2011). By using different number of passes and chamber sizes within the homogenizer, the fiber morphologies can be varied, i.e. with decrement or increment in number of passes the thicker fibers (MFC) or thinner fibers (NFC) are produced (Abdul Khalil et al. 2012). Finally, the processed suspension contains a heterogeneous mixture of MFC/NFC fibers with different diameter and aspect ratio. The composition of the fibrils and the homogeneity of the fibril size distribution will further affect the rheological properties of MFC/NFC suspensions (Taheri and Samyn 2015).

After processing through the homogenizer, the fibers form a gel-like suspension with a stepwise increment in viscosity due to strong interfibrillar forces, as observed e.g., for TEMPO-oxidized fibers (Pääkkö et al. 2007; Lasseuguette et al. 2008). The interfibrillar forces result in variations of rheological behavior for MFC/NFC suspension that are essential to control (Dinand et al. 1996; Iotti et al. 2011). However, other works describe an increment of viscosity followed by decreases of viscoelastic properties as the number of passes in the homogenizer increases, resulting in weaker gels (Shogrena et al. 2011; Benhamoua et al. 2013). One of the reasons of decrement of viscoelastic behavior (besides the increase of negative electrostatic charge) is a decrease of the aspect ratio (Li et al. 2015). The non-uniform MFC/NFC suspension has a tendency to become instable: (1) flocculation occurs when thicker fibers are entangled into a thinner fiber network and form big flocs, while (2) aggregation of single cellulose microfibrils occurs through the interaction of thin fibers. Therefore, stabilizing agents (e.g., $NaClO_2$) help to overcome a critical challenge during MFC/NFC extraction and lead to a uniform production of fibers with high surface area (Iwamoto et al. 2008). The entanglement of the fibrillated fiber network widely influences the rheological properties such as zero-shear viscosity, yield stress, shear thinning and shear thickening, which can be altered by the amount of fibrillation (Saito et al. 2006). The fiber network is responsible for the gel-like behavior of MFC/NFC

suspensions even at low concentrations. Moreover, the settlement and flocculation of fibrils within the network affect the yield stress and provide a power-law correlation between storage modulus and concentration (Tatsumi et al. 2002; Ono et al. 2004; Hill 2008; Lasseuguette et al. 2008). The fibril diameter and fibrillation directly affect the colloidal and non-colloidal behavior of MFC/NFC suspension at macroscopic (volume fraction and rotation of the fibers) and microscopic (electrostatic interactions between fibers) scale (Saarikoski et al. 2012), and contributes to the flocculation (Hubbe 2007; Mewis and Wagner 2009). The higher viscosity of NFC suspensions compared to MFC suspensions at equivalent concentration is related to a higher number of hydrogen interactions and/or more important fiber entanglement (Missoum et al. 2010). The rheological response of MFC/NFC suspensions, such as aggregation/flocculation and viscosity over different shear rates or at rest, is essential information for better control of the processing and mixing of MFC/NFC in future biocomposite applications. Therefore, good insight in the relation between fiber morphology and rheological properties of the fiber suspension should be established. Moreover, the application of shear may induce a "memory" or "time-dependent" effect with retarded strain recovery after creep due to the visco-elastic properties of the suspension, which has not yet been widely detailed.

In this work, the effect of mechanical processing (homogenization and/or microfluidization) of fibrillated cellulose within different chambers and number of passes on rheological behavior was detailed in order to optimize the processing steps providing stable fiber suspensions. As the fiber content is another primary factor affecting the rheology properties of the fiber suspension (Charani et al. 2013; Chen et al. 2013), the fiber concentration has been kept constant. Besides traditional rotational and oscillatory rheology testing, the viscoelastic behavior of the suspensions was further detailed and better understood by fitting experimental creep and strain recovery data to the phenomenological Burger model. Furthermore, the apparent yield stress has been determined from the Herschel–Bulkley equation and can be related to the formation and breakage of the fiber network and fiber entanglements (Barnes 1999; Masalova et al. 2008; Derakhshandeh et al. 2010). Although it is sometimes difficult to quantify the MFC/NFC morphology and correlate it to rheological behavior, a unique relationship between processing

parameters and rheological properties is presented by introducing the total number of passes, Péclet number and zeta potential as representative parameters for the suspension characteristics.

## Experimental

Materials and sample preparation

Starting from never dried hard wood kraft pulp (Stora Enso, Finland), MFC/NFC suspensions were obtained by processing a 0.5 wt% diluted pulp suspension under high pressure/shear rate in a M-110EH Microfluidizer (Microfluidics, USA). The fiber suspensions have been sonicated for 15 min before processing to avoid chamber blockage or clogging.

The sample preparation was designed in four different groups with use of three different chamber sizes including a homogenizer chamber (H210 Z-shaped with pressure of 500 bar), 200 μm interaction chamber (H30 Z-shaped with pressure of 1000 bar) and 87 μm interaction chamber (G10 Z-shaped with pressure of 1500 bar). Two different chambers can be connected serially or in case of using a single chamber, the other chamber can be substituted with a normal flow tube. As shown in Table 1, the samples H1–H3 and S1–S9 have been processed with a combination of different chambers and passes. According to this processing protocol, comparing a sample with an optimum number of passes

from each group presents comparative data about the effect of chamber size on rheological behavior: the effect of number of passes can be seen by comparing (S2, S4, S5, S6), while the effect of chamber size can be seen by comparing (H2, S5, S8). The optimum number of passes in each group has been selected based on microscopy or zeta potential data, providing suspensions with desired properties (i.e. fiber homogeneity and lowest zeta potential value (see later)).

Sample characterization

The stability of the suspensions and surface charges of the fibers have been characterized by zeta potential values, measured with a Zetasizer Nano ZS90 (Malvern, UK) at 25 °C using a capillary cell (DTS 1060, Malvern, U.K).

The morphology of fibrillated cellulose has been studied by scanning electron microscopy (SEM) and atomic force microscopy (AFM). A diluted droplet of the MFC/NFC suspension was dried overnight on freshly cleaved mica and characterized by SEM (Tabletop microscope TM 3000, Hitachi, Krefeld, Germany). The AFM measurements were obtained on a Nanoscope III with a tube scanner from Digital Instruments (Veeco, Santa Barbara, CA, USA) and AFM tips with radius of curvature less than 10 nm, stiffness of k = 50 N/m and frequency of 300–350 kHz (PPP-NCH, Nanoandmore, Wetzlar, Germany). A non-diluted droplet of the MFC/NFC suspension was placed

**Table 1** Process conditions of MFC/NFC suspension samples in four different groups with use of 0.5 wt% pulp suspension

| Group | Sample name | Number of passes within (H210Z) homogenizer chamber with constant pressure of 500 bar | Number of passes within (H30Z) 200 μm chamber with constant pressure of 1000 bar | Number of passes within (G10Z) 87 μm chamber with constant pressure of 1500 bar |
|---|---|---|---|---|
| 1 | H1 | 20 | N/A | N/A |
| | H2 | 25 | N/A | N/A |
| | H3 | 30 | N/A | N/A |
| 2 | S1 | 20 | 10 | N/A |
| | S2 | 25 | 10 | N/A |
| | S3 | 30 | 10 | N/A |
| 3 | S4 | 25 | 5 | N/A |
| | S5 | 25 | 15 | N/A |
| | S6 | 25 | 20 | N/A |
| 4 | S7 | 25 | 15 | 5 |
| | S8 | 25 | 15 | 10 |
| | S9 | 25 | 15 | 15 |

on a carbon-coated copper grid for observation by transmission electron microscopy (TEM) (Zeiss LEO CEM 912) operating at 100 kV accelerating voltage.

The crystalline structure of fibrillated cellulose was studied after freeze-drying the MFC/NFC suspension samples (H2, S2, S5 and S8) for 48 h. The samples were converted into pellets that were compressed in a hydraulic press with prescribed pressure of 170 MPa. The Wide Angle X-ray Diffraction (WAXD) measurements were done with a STOE diffractometer (Darmstadt, Germany, STADI-P) using Cu K$\alpha$1 (wavelength 1.54056 Å) as a radiation source at 40 kV and 30 mA, and patterns were recorded in the range $2\theta = 5°$–$40°$ at $0.6°$/min with a $0.01°$ resolution. No further background corrections were made. The Miller indices were assigned to the diffraction peaks according to recommended conventions for the unit cell dimensions of cellulose I (French 2014). An estimation for the cellulose crystallinity was made by calculating the crystallinity index ($CrI_1$) following the Segal method (Segal et al. 1959), according to Eq. (1):

$$CrI_1(\%) = \frac{(I_{200} - I_{am})}{I_{200}} \times 100 \qquad (1)$$

with $I_{200}$ the maximum intensity of the diffraction peak at $2\theta = 22.5°$ corresponding to (200) and $I_{am}$ the minimum in intensity at around $2\theta = 18°$ representing the amorphous fraction for cellulose I$\beta$.

The chemical composition of freeze-dried samples (H2, S2, S5 and S8) was further studied by attenuated total reflection Fourier-transform infrared spectroscopy (ATR-FTIR) (Spectrum 65, Perkin Elmer), measuring spectra at 4000–550 cm$^{-1}$ with a resolution of 4 cm$^{-1}$ and averaged over 32 scans. The crystallinity index ($CrI_2$) was calculated as the average of the absorbance ratio of 1372 cm$^{-1}$ ($A_{1372}$) over 2900 cm$^{-1}$ ($A_{2900}$) or $A_1$, and the absorbance ratio of 1430 cm$^{-1}$ ($A_{1430}$) over 893 cm$^{-1}$ ($A_{893}$) or $A_2$ (Salmén et al. 2005), according to Eq. (2):

$$CrI_2(\%) = \frac{(A_1 + A_2)}{2} \times 100 \qquad (2)$$

Rheometry and methods

A cylindrical rheometer (Haake Mars III, Thermo Scientific, Germany) with a bob (CC25 DIN Ti with radius 12.54 mm) and cup (CCB DIN TM-PE-C with radius of 13.60 mm) rotational system was used for rheological tests of MFC/NFC suspensions at 25 °C. For each experiment, 16.1 ml of suspension was loaded into the cup with smallest stress to eliminate history or memory effects. The gap distance of 2.1 mm was slowly adjusted during 2 min to erase additional stress and equilibrate the temperature between sample and cup. During testing, water evaporation of the suspensions was eliminated by using a standard hood-glass cover. The rheometry tests were designed in three different protocols with steady-state rotational, creep & strain recovery, and oscillatory testing. The rotational measurements were done under controlled shear rate in a ramp-up/ramp-down sequence to show the suspension stability at shear rates 1 to 1500 s$^{-1}$ (within 15 min) at 25 °C. The wall slip effect and reproducibility were checked under ramp-up and ramp-down shear rates (15 min ramp-up + 15 min ramp-down) between 10 and 1500 s$^{-1}$ for a single sample. The wall slip phenomenon might be indicative for instabilities in shear-viscosity plots (Bröckel et al. 2013; Nechyporchuk et al. 2014) and can be assessed by changing the gap distance: by preliminary testing, the MFC/NFC suspensions did not show wall slip or viscosity differences of more than 0.5 Pa s at gap distances of 1.5, 2.1 and 2.7 mm (see supplementary information SI1). The creep tests were done at a shear stress of 1 Pa for the first samples group (H1, H2 and H3) over a time of 300 s at constant temperature of 25 °C and the strain recovery was recorded after unloading of stress over a time of 900 s. The same creep (over 300 s) and strain recovery (over 900 s) protocol was applied to the second samples group (S1, S2 and S3) and third samples group (S4, S5 and S6) at shear stresses of 2 and 5 Pa. This test was also done for the fourth samples group (S7, S8 and S9) at shear stresses of 2, 5 and 20 Pa. The different stresses during creep were selected to show the viscoelastic or viscous behavior at low stress and high stress, respectively. The oscillatory data were measured under strain sweep (strain interval from 0.001 to 100 % at constant frequency 0.1 Hz) and frequency sweep (frequency interval from 0.1 to 100 rad.s$^{-1}$ at constant strain 0.05 %) modes at 25 °C. The oscillatory test was used to indicate the gel-like and liquid-like transition region at the cross-over point of storage modulus ($G'$) and loss modulus ($G''$).

## Results and discussion

### Microscopy and zeta potential

The morphology of MFC/NFC fibers was observed by SEM and AFM to determine the diameter of the fibers and homogeneity of the samples, as shown in Figs. 1 and 2. As seen from the micrographs, the samples contain a mixture of MFC and NFC fiber morphologies. With ongoing processing, an increasing amount of fibrillation is observed as a reduction in fiber diameter (Henn and Fraundorf 1990). The fiber diameter range has been determined as an average from 10 micrographs. With use of zeta potential values, the stability of the suspensions was judged. The fiber diameters and zeta potential values for all samples are summarized in Table 2. In this discussion, samples of each group are first separately evaluated and then the samples processed under optimum conditions (H2, S2, S5 and S8) are compared:
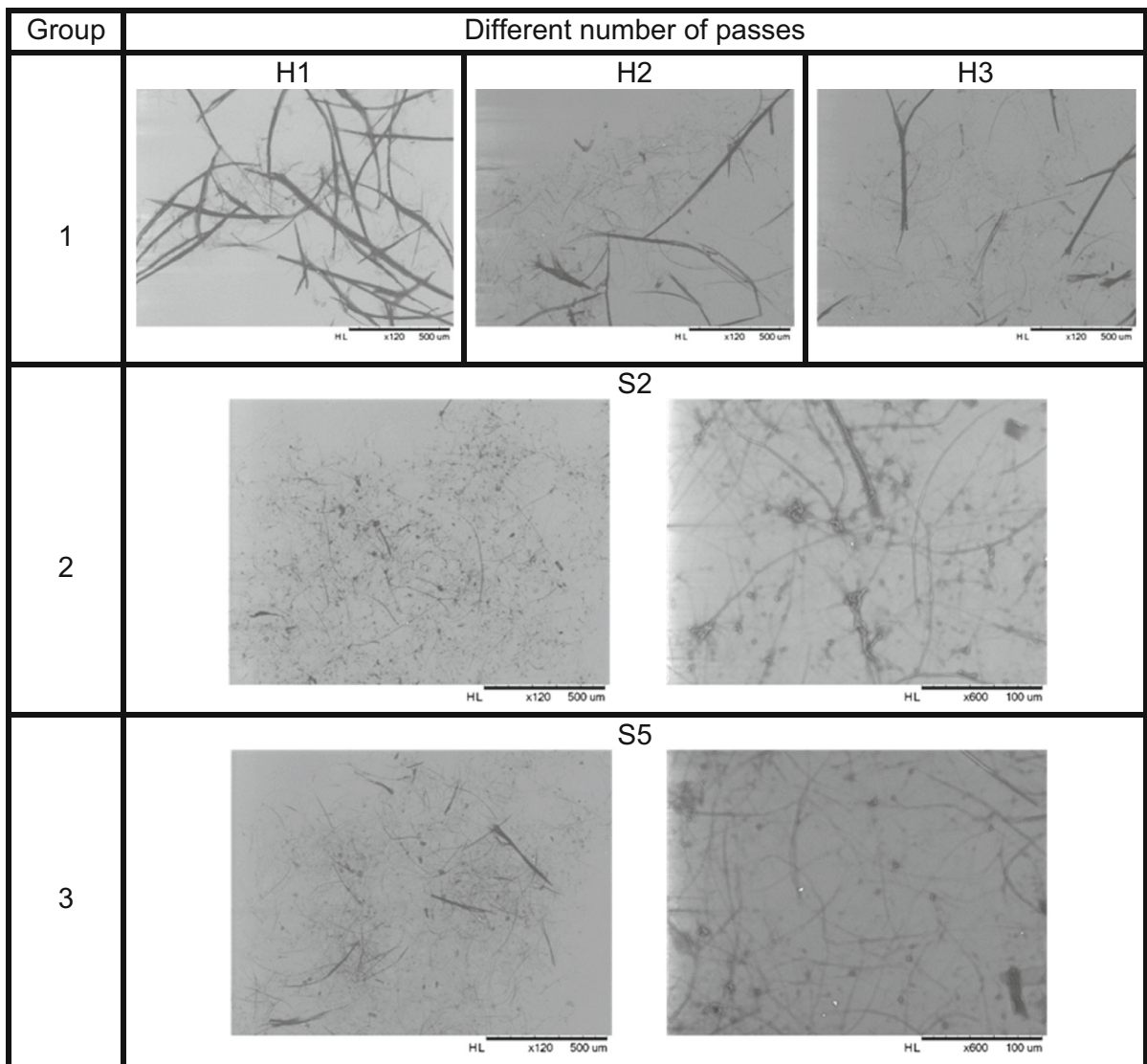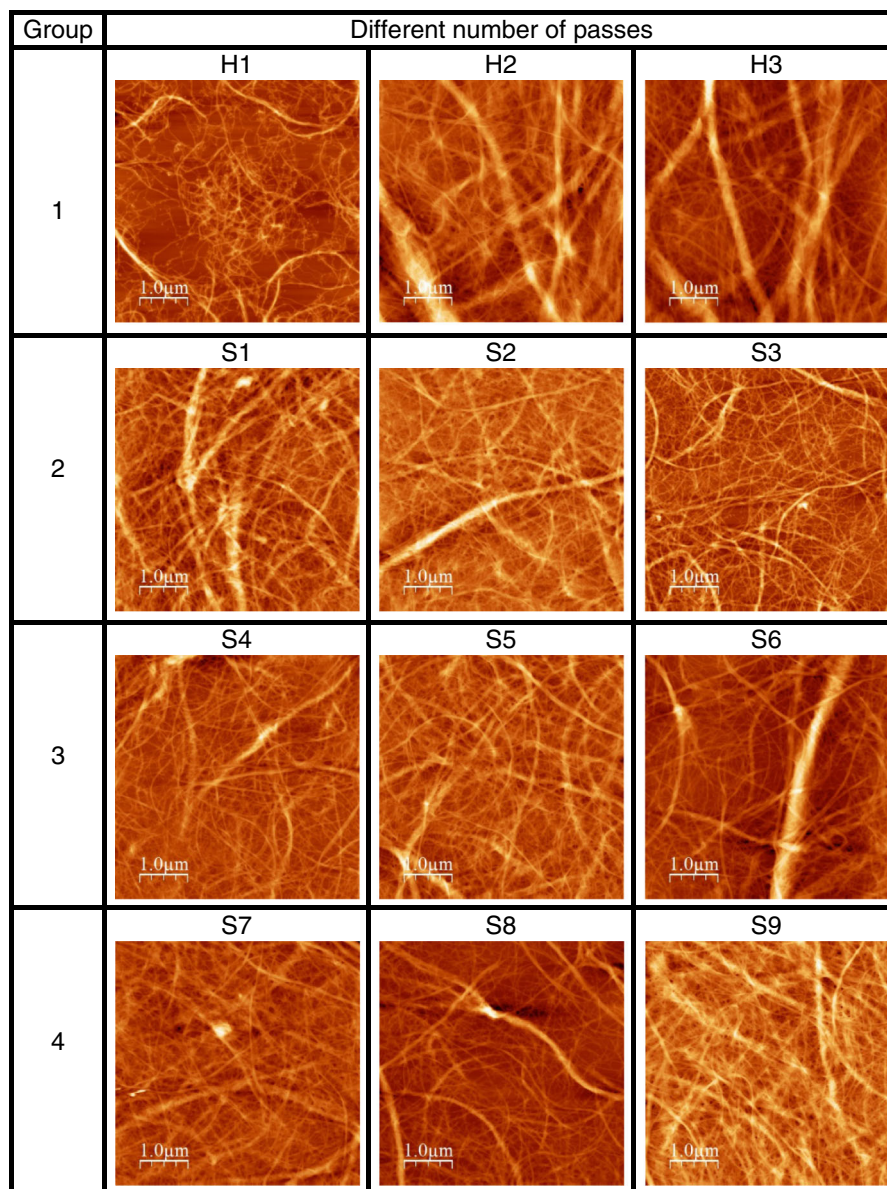


**Fig. 1** Scanning electron microscopy (SEM) of MFC/NFC suspensions processed within different interaction chambers and with different number of passes

**Fig. 2** Atomic force microscopy (AFM) of MFC/NFC suspensions processed within different interaction chambers and with different number of passes



- Group 1 (H1, H2 and H3): The number of passes in the homogenizer chamber has an important effect on homogeneity of the MFC/NFC suspensions, as the amount of thick fibers decreased and the maximum fiber diameter range changed from 45 to 20 μm with increment of number of passes (SEM). According to AFM images, however, the minimum fiber diameter range did not decrease below 45 nm with higher number of passes. Therefore, the minimum diameters after processing in the homogenizer chamber did not depend on the

number of the passes but was primarily limited by the size of chamber. The zeta potential values show a primary increment of negative electrical charge (−39.3 to −48.8 mV) and secondary decrement (−48.8 to −45.7 mV) with number of passes, which can be related to fibrillation (H1, H2) and flocculation (H3), respectively.

- Group 2 (S1, S2 and S3): By changing the number of passes in the homogenizer chamber followed by a constant number of passes in the 200 μm interaction chamber, the homogeneity of the suspension

**Table 2** Zeta potential and fiber diameter range for MFC/NFC suspension samples (*SD* standard deviation)

| Group | Sample name | Zeta potential ± SD (mV) | Minimum diameter from AFM (nm) | Maximum diameter determined from SEM*, TEM** or AFM*** |
|-------|-------------|--------------------------|-------------------------------|--------------------------------------------------------|
| 1 | H1 | −39.3 ± 1.25 | 45 | 45 μm* |
|   | H2 | −48.8 ± 0.81 | 45 | 25 μm*, 5 μm** |
|   | H3 | −45.7 ± 1.14 | 45 | 20 μm* |
| 2 | S1 | −50.1 ± 1.13 | 20 | 15 μm* |
|   | S2 | −63.2 ± 1.34 | 20 | 9 μm*, 100 nm** |
|   | S3 | −52.3 ± 1.97 | 20 | 7 μm* |
| 3 | S4 | −61.3 ± 1.51 | 20 | 10 μm* |
|   | S5 | −66.7 ± 1.62 | 20 | 5 μm*, 100 nm** |
|   | S6 | −53.7 ± 1.64 | 20 | 3 μm* |
| 4 | S7 | −62.2 ± 0.49 | 15 | 60 nm*** |
|   | S8 | −67.0 ± 1.02 | 15 | 55 nm**, 50 nm*** |
|   | S9 | −53.5 ± 1.18 | 15 | 35 nm*** |

The fibers diameter was extracted from SEM (*), TEM (**) and/or AFM (***) data

improved and the thick fibers were further fibrillated with a decrease in maximum fiber diameter from 15 to 7 μm at higher number of passes (SEM). From AFM images, the minimum fiber diameter range did not decrease below 20 nm. In general, the use of a 200 μm interaction chamber favors the production of a more uniform suspension. The zeta potential values show a primary increment (−50.1 to −63.2 mV) and secondary decrement (−63.2 to −52.3 mV), which can be related to ongoing fibrillation of fibers (S1, S2) and aggregation (S3), respectively.

- Group 3 (S4, S5 and S6): By changing the number of passes in the 200 μm interaction chamber for a constant number of passes in the homogenizer chamber, the thick fibers were progressively fibrillated with a decrease in maximum fiber diameter of 10–3 μm (SEM). The AFM images showed no reduction in minimum fiber diameter below 20 nm. The variation in zeta potential values with a primary increment (−61.3 to −66.7 mV) and secondary decrement (−66.7 to −53.7 mV) can systematically be related to fibrillation (S4, S5) and aggregation (S6). By comparing the samples (S4, S5, S6) with the sample (S2) from the second group, a monotoneous trend in fiber diameter reduction and zeta potential reduction with increasing number of passes in the 200 μm chamber is noticed. However, the homogeneity of the suspension relates to the number of passes in the 200 μm chamber, as a too high number of processing steps deteriorates the quality of the suspension.

- Group 4 (S7, S8 and S9): By altering the number of passes in the 87 μm interaction chamber with a constant number of passes within the homogenizer chamber and 200 μm chambers, fibers were not visible in SEM due to very fine fibrillation. The AFM images showed that the maximum fiber diameter was further reduced from 60 to 35 nm, but the minimum fiber diameter did not decrease below 15 nm. The zeta potential values show similar a trend as other groups with a primary increment (−62.2 to −67.0 mV) and decrement (−67.0 to −53.5 mV), due to aggregation for the sample with highest number of passes (S9).

Comparing the samples with optimum processing conditions within each group (H2, S2, S5 and S8 with highest zeta potential), a monotonous diameter reduction from 25 μm to 50 nm for thick fibers and from 45 to 15 nm for thin fibers is in parallel with the progressive increase in zeta potential values from −48.8 to −67.0 mV. In conclusion, the use of smaller chamber sizes with an optimum number of passes improves the quality of the suspension in terms of increasing of zeta potential. On the other hand, an increase in the number of passes behind the optimum value decreases the zeta potential because of aggregation. An increase in number

of passes per chamber further reduces the maximum fiber diameter and results in a suspension with more uniform fiber diameter. Meanwhile, the minimum fiber size depends on the size of the interaction chamber while it does not depend on the number of passes within that chamber. However, it has to be noticed that SEM and AFM images represent local observations of the fiber morphology and are characteristic for the dry fiber state, while the flow behavior of the overall suspensions might rather depend on the overall amount of fibrillation, aspect ratio distribution and long-range ordering. In this regard, zeta potential values are more representative for the MFC/NFC fibers in suspension and will be further considered in relation with rheological characteristics.

Due to the eventual aggregation of MFC/NFC fibers by hydrogen-bonding during the drying process, the genuine morphology and size of MFC/NFC fibers with optimum processing conditions within each group (H2, S2, S5 and S8) were further evaluated by TEM, as shown in Fig. 3. The TEM images elucidate that processing within the homogenizer chamber (H2) results in a MFC/NFC suspension with low proportion of MFC and high proportion of NFC, while processing within the smaller microfluidizer chambers (S2, S5 and S8) result in a nearly pure NFC suspension with high proportion of NFC. The fiber diameters for samples under optimum processing conditions (H2, S2, S5 and S8) were determined from TEM and are listed in Table 2.

Crystallinity of fibrillated cellulose fibers

Based on Wide Angle X-ray Diffraction (WAXD) measurements, the crystallinity of samples with optimum processing conditions (H2, S2, S5 and S8) has been evaluated. The experimental WAXD patterns (see supplementary information SI2a) show diffraction peaks for MFC/NFC samples at $2\theta = 16.1°$ for a combination of (1–10) and (110), and $2\theta = 22.4°$ and $34.5°$ that correspond to (200) and (004) crystallographic planes of cellulose I$\beta$.

Based on FTIR spectra, variations in fibrillation and crystallinity of samples (H2, S2, S5 and S8) together with native cellulose pulp (R) can be distinguished (see supplementary information SI2b) after normalization at the 1160 cm$^{-1}$ band corresponding to C–O–C stretching (Kataoka and Kondo 1998). A full spectroscopic analysis is beyond the scope of this study, while only most relevant influences of processing are illustrated.

The broad band at 3600–3100 cm$^{-1}$ corresponds to OH stretching due to hydrogen bonds (Adebajo and Frost 2004; Kondo 1997), which however does not provide quantitative data about the MFC/NFC samples [mainly not in case of highly different amounts of fibrillation comparing R, H2 and (S2, S5, S8)], because of aggregation under drying. It only is noticed that the intensity of the more fibrillated sample (S8) is higher than (S2, S5), which can be correlated with the scission of the intra- and intermolecular hydrogen bonds under shear by using a smaller chamber. Otherwise, the single band at 2900 cm$^{-1}$ corresponding to the C–H stretching splits into two separate bands under more intense processing and increment in intensities (S2, S5) < S8, depending on chamber size. Both observations are typical for the occurrence of more amorphous cellulose developing during processing (Karande et al. 2011), which seems to be more sensitive to the chamber size than number of passes. The fingerprint region for cellulose at 900–1100 cm$^{-1}$ strongly varies with processing, characterized by a gradual broadening in the 970 cm$^{-1}$ shoulder with higher total number of processing steps as most important trend, related to the formation of amorphous structure and conformational changes in the cellulose backbone by internal fibrillation (Janardhnan and Sain 2011). In addition, the band appearing at 1035 cm$^{-1}$ has been attributed to OH groups in glucose units (Kacuralova et al. 2000), which likely may be exposed more gradually upon shear processing. The absorbance band at 1430 cm$^{-1}$ corresponds to a symmetric CH$_2$ bending and is referred to as a "crystallinity band" (Oh et al. 2005): the band increases sharply after first homogenization step due to abrupt reorganization of the structure, but further decrements in intensity indicate a reduction in crystallinity with intensities (S2, S5) < S8 < H2. This variation is even more clear at the absorbance band 1458 cm$^{-1}$ band, representing the C–OH group. As such, the variations in crystallinity seem to relate mostly to the change in chamber size, while the increase in number of passes is of secondary influence. In parallel, the variations in the absorbance band at 893 cm$^{-1}$ related to C–O–C stretching as a characteristic "amorphous band" (Nelson and O'Connor 1964) show a progressive increase in amorphous phase after processing, with highest intensity for sample S8. The decrease in crystalline phase and increase in amorphous phase with processing might not fully correlate due to presence of a semi-oriented nematic phase (Kondo et al. 2001).

**Fig. 3** Transmission electron microscopy (TEM) of MFC/NFC suspensions processed within different interaction chambers and with different number of passes
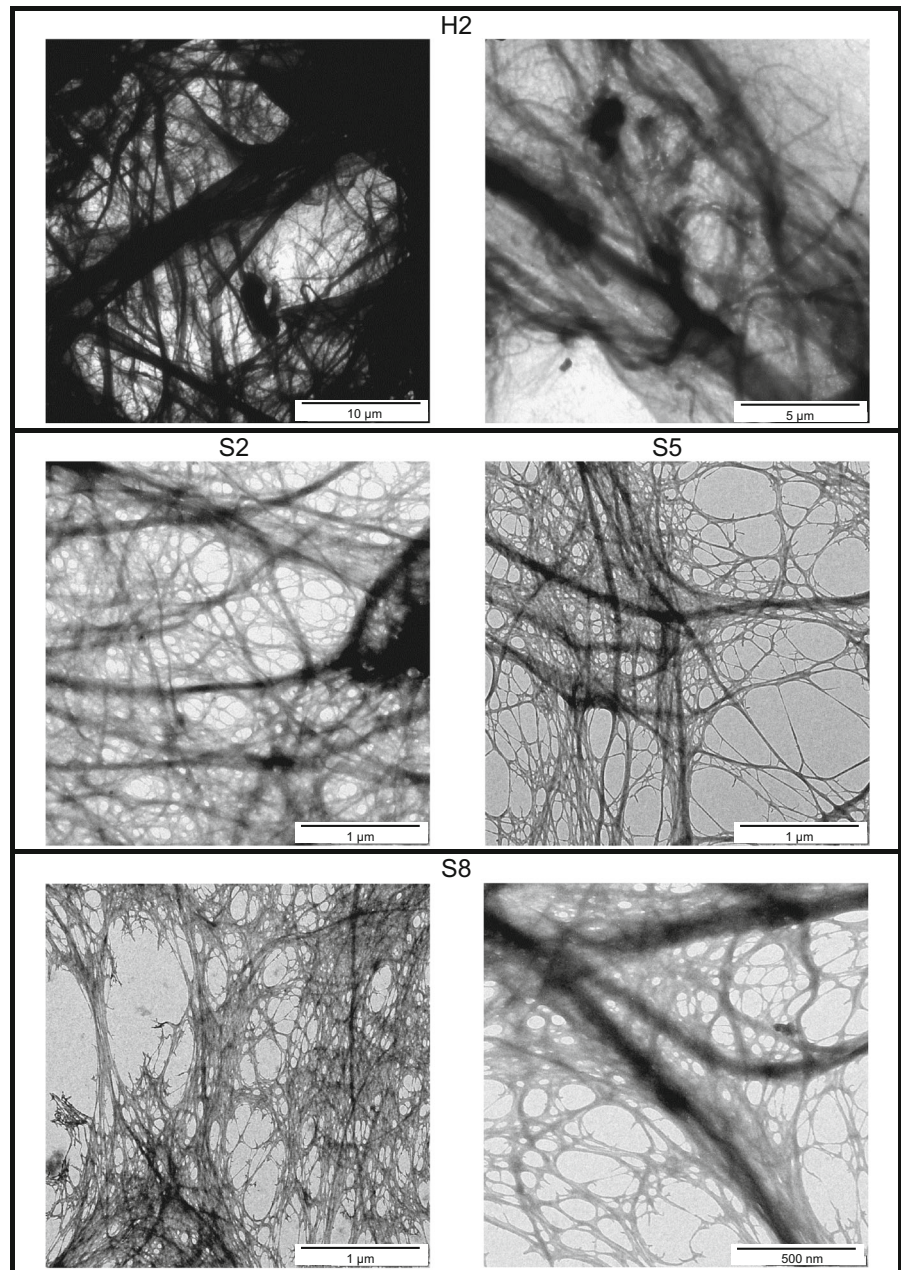


The crystallinity index $CrI_1$ calculated from WAXD data [see Eq. (1)] and $CrI_2$ calculated from FTIR data [see Eq. (2)] is given in Table 3. By comparing crystallinity index $CrI_1$ (from WAXD) and $CrI_2$ (from FTIR), there is a parallel trend of decreasing crystallinity with using smaller interaction chambers of 200 and 87 μm (e.g., samples H2, S2, S8). Similar findings of decrease in crystallinity by high pressure disintegration were reported by means of

X-ray diffraction (Iwamoto et al. 2007). This can be related to an alteration of crystallinity under high mechanical shear forces and consequent frictional forces on the crystalline regions within the thinner interaction chamber. Alternatively, crystallinity index $CrI_1$ (from WAXD) and $CrI_2$ (from FTIR) show the same trend of increment in crystallinity with higher number of passes with using the same interaction chamber (e.g., samples S2 and S5), which might be

**Table 3** Crystallinity index of cellulose micro- and nanofibers calculated from WAXD data ($CrI_1$) and FTIR data ($CrI_2$)

| Sample name | Crystallinity index | |
|---|---|---|
| | $CrI_1$ (%) | $CrI_2$ (%) |
| H2 | 71.5 ± 0.1 | 72.0 ± 0.1 |
| S2 | 61.3 ± 0.1 | 66.9 ± 0.1 |
| S5 | 65.6 ± 0.1 | 69.1 ± 0.1 |
| S8 | 62.0 ± 0.1 | 60.0 ± 0.1 |

explained by a decrease in the random amorphous phase by orientation of smectic regions under shear. The differences in absolute values between $CrI_1$ and $CrI_2$ may be related to the presence of a nematic phase that can either be seen as a crystalline or amorphous state by different characterization methods.

Rotational rheology

The steady-state data for viscosity versus shear rate under controlled shear rate mode are compared for samples from the first group (H1, H2, H3 processed with homogenizer chamber) in Fig. 4a and third group (S4, S5, S6 processed with different number of passes in the 200 μm chamber) in Fig. 4b. The viscosity trends for samples from second group (S1, S2, S3) and fourth group (S7, S8, S9) show the same behaviors (see supplementary information SI3).

- For the first group H1, H2, H3 (Fig. 4a), the ascending shear rate data show primary shear thinning and secondary shear thickening effects with high viscosity fluctuations. The shear thinning happens when the suspension network flows within a low shear rate interval. However, the shear thickening at intermediate shear rates might be caused by flocculation of thick fibers and the viscosity fluctuations at high shear rates might happen by packing/flowing of thick and thin fibers. The visual observation also showed accumulation of big flocs on the surface of the cup, which might happen while the secondary flow at high shear rate pushes the flocs towards the top of the cup. This behavior demonstrates the instability of MFC/NFC suspensions and is in agreement with inhomogeneous morphology of H1, H2 and H3 samples described before. The descending shear rate data show minimum viscosity fluctuations while the flocs formed under high shear stress were not removed but rather disentangled.
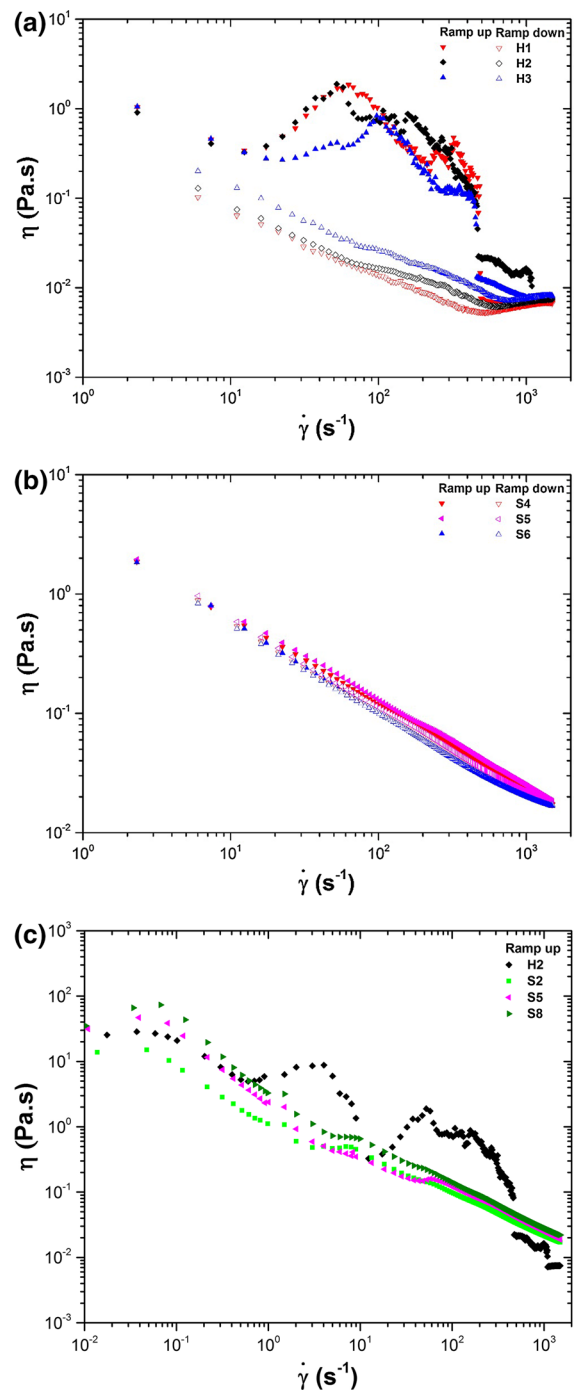
**Fig. 4** Shear rate versus viscosity plots of MFC/NFC suspensions (0.5 wt%) at 25 °C: **a** H1, H2 and H3 processed within homogenizer chamber, **b** S4, S5 and S6 processed within homogenizer and 200 μm chambers, **c** comparison of ascending shear rate versus viscosity plots of MFC/NFC suspensions (0.5 wt%) at 25 °C for optimum processed samples. The *solid symbols* are from ascending shear rate and the *open symbols* are from descending shear rate

- For the third group S4, S5, S6 (Fig. 4b), strong linear shear thinning was observed for samples that were processed within the homogenizer chamber, 200 and/or 87 μm chambers, in parallel with other literature (Lowys et al. 2001; Iotti et al. 2011). Moreover, the small hysteresis comparing ramp-up/ramp-down tests demonstrates the good morphological homogeneity of the samples. A general increase in viscosity trend form S4 to S5 and decrease in viscosity trend from S5 to S6 is observed, which agrees with the evolution of zeta potential values. Therefore, an optimum number of processing passes leads to the increment of viscosity (in parallel with zeta potential and amount of fibrillation), while a higher number of processing passes might decrease these parameters because of aggregation.

In general, the structure of NFC/MFC suspensions alters at higher shear rate (Björkman 2003). While flocculated fiber networks can form by fibrils at rest, the networks rupture to form chain-like flocs under low shear rates and form large flocs at high shear rates. Therefore, optimum processing conditions of the MFC/NFC suspensions should provide an optimum fiber network morphology with smooth rheological characteristics. The viscosity versus shear rate plots for optimum processed samples (H2, S2, S5 and S8) within a broader shear rate interval $10^{-2}$ to $10^{3}$ s$^{-1}$ (within 30 min) are shown in Fig. 4c. The viscosity trend for H2 becomes somewhat more stable at very low shear rates, but it remains highly fluctuating at high shear rates as an indication for flocculation. The viscosity trends for S2, S5 and S8 show a transition region with a Newtonian plateau at intermediate shear rates 2–40 s$^{-1}$, representative for the aggregation of MFC/NFC suspensions. The aggregation can occur at intermediate shear rates (e.g., S2, S8) or at higher shear rates (e.g., S5) during a ramp up test, while breaking up again at higher shear rates. Thus, it can be assumed that samples with high homogeneity tend to dynamically aggregate or flocculate under certain conditions of shear rate while becoming homogeneous again under high shear rates, which is characteristic for fibrillated cellulose suspensions (Karppinen et al. 2012; Saarikoski et al. 2012).

The shear rate and shear stress data from rotational rheometry were used to determine the apparent yield stress of MFC/NFC suspensions, which is related to the onset of flow. The flow behavior of a fluid is related to the yield stress in a non-linear way according to the Herschel–Bulkley model given in Eq. (3),

$$\tau = \tau_0 + k(\dot{\gamma})^n \qquad (3)$$

with parameters $k$ (consistency), $n$ (flow index) and $\tau_0$ (apparent yield stress). The equation does not describe the Newtonian plateau at intermediate shear rates (Karppinen et al. 2011), and fits can only be done at shear rates above the transition region between 50 and 500 s$^{-1}$, as shown in Fig. 5a. These fits were used to define the effect of chamber size and the number of the passes on the apparent yield stress for MFC/NFC suspensions: as concluded from Fig. 5b, the size of the chamber has more influence on the increment of yield
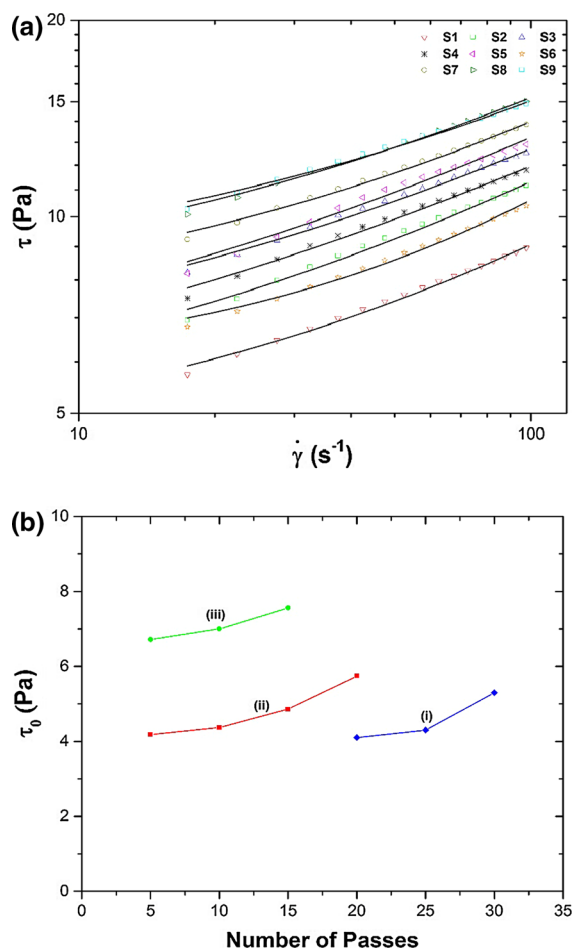


**Fig. 5** Description of yield stress for MFC/NFC suspensions, **a** Herschel–Bulkley fits of different MFC/NFC suspensions (0.5 wt%) within ramp-up test at 25 °C, **b** effect of chamber type and number of passes on apparent yield stress of MFC/NFC suspensions, (*i*) group 2 (*ii*) group 3 (*iii*) group 4

stress compared to the number of passes. Therefore, the MFC/NFC suspensions (S7–S9) processed in the 87 μm chamber show higher yield stress, which can be related to the onset of flow at higher stress for samples with a more entangled fiber network.

The relation between rheological properties (viscosity) and processing conditions (total number of passes) of MFC/NFC suspensions is further assessed by introducing the rotational Péclet number as a dimensionless quantity that explains the contributions of size, rheological parameters, Brownian and hydrodynamic forces by the following Eq. (4) (Bröckel et al. 2013):

$$Pe_{rot} = \frac{8\pi a^3 \eta}{3k_B T(\ln 2l/2a - 0.5)} \dot{\gamma} \qquad (4)$$

where $a$ and $l$ are the diameter and length of fibers, $k_B T$ is the thermal energy, $\eta$ is viscosity and $\dot{\gamma}$ is shear rate. As shown in Fig. 6, the effect of total number of passes versus rotational Péclet number for MFC/NFC suspensions is plotted ($R^2 = 0.985$) at zero shear viscosity for $l = 2$ μm and fiber diameters determined in Table 2. Thus, an increment of the number of passes results in a higher rotational Péclet number, which can interestingly serve as a unique parameter that directly relates the morphology and rheological behavior of MFC/NFC suspensions at low shear rate/shear stress. The aspect ratio of fibers can be altered within processing conditions. As the variations were more pronounced for diameter reduction comparing to
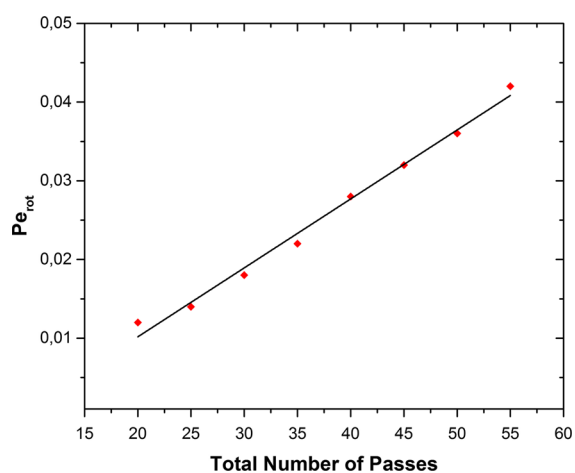
length reduction (1–3 μm), a constant length of fibers ($l = 2$ μm) has been assumed for all rotational Péclet number calculations.

Creep and strain recovery

The creep and strain recovery of MFC/NFC suspension were measured for samples from different groups: the suspensions show elastic, viscoelastic or purely viscous behavior depending on the applied shear stress. Therefore, creep and strain recovery was measured at stresses where the suspension behaves either like a viscoelastic or viscous material, i.e. 1 Pa for the first group (Fig. 7), 2 and 5 Pa for the second group (Fig. 8) and third group (see supplementary information SI4), or 2, 5 and 20 Pa for the fourth group (Fig. 9).

- For the first group H1, H2, H3 (Fig. 7), the suspension behaves viscoelastically at 1 Pa. The number of passes within the homogenizer chamber directly influences the maximum compliance and the recovery part. Therefore, the lower number of passes results in larger creep compliance for H1 due to low amount of fibrillation. Unlikely, the increment of the number of passes results in a lower creep compliance for H2 or H3 related to the higher amount of fibrillation and network formation. Moreover, the suspensions show more recovery with higher number of passes. The creep and strain recovery at low stress correspond to the gel-
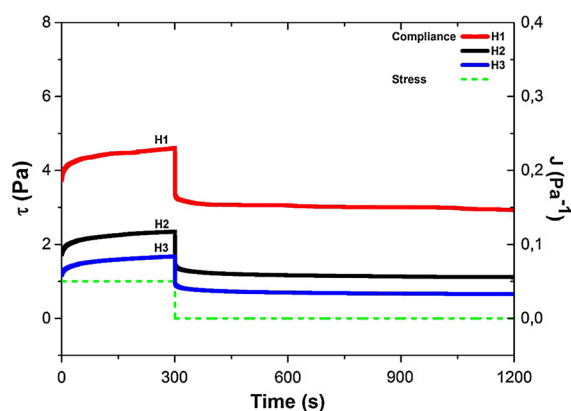


**Fig. 6** Relation between total number of passes during mechanical processing of MFC/NFC suspensions (0.5 wt%) in microfluidizer versus rotational Péclet number (Pe)



**Fig. 7** Creep (stress 1 Pa) for $t_{Creep} = 300$ s and strain recovery (zero stress) for $t_{Recovery} = 900$ s at 25 °C for MFC/NFC suspensions (0.5 wt%) processed within homogenizer chamber
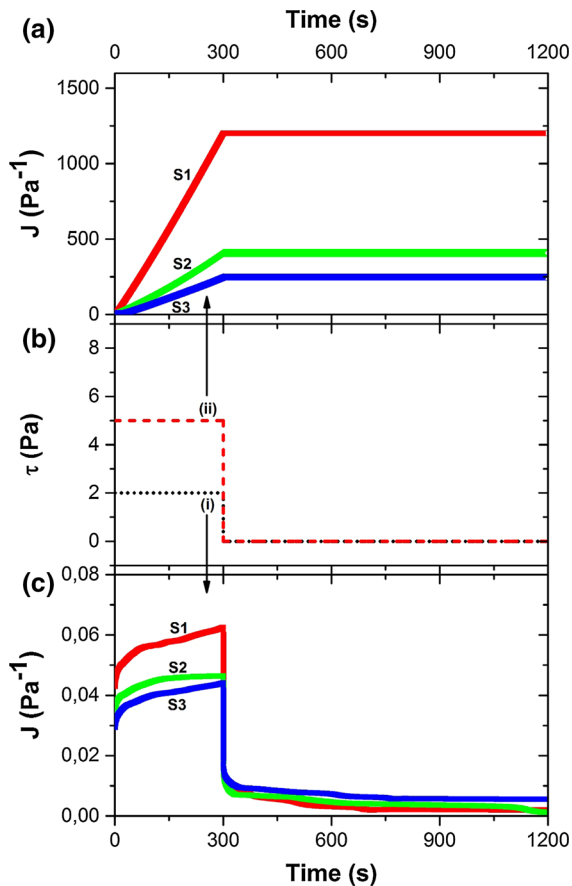
**Fig. 8** Creep and strain recovery test of MFC/NFC suspensions (0.5 wt%) processed within homogenizer and 200 μm chambers; **a** creep and strain recovery compliance versus time at stress 5 Pa, **b** stress versus time, **c** creep and strain recovery compliance versus time at stress 2 Pa. Tests were done for $t_{Creep}$ = 300 s and strain recovery (zero stress) for $t_{Recovery}$ = 900 s at 25 °C

like behavior of the suspension. For this group, however, the stresses higher than 1 Pa resulted in strong fluctuation of the creep compliance, which is not further considered.

- For the second group S1, S2, S3 (Fig. 8), the suspensions show viscoelastic behavior at 2 Pa and viscous behavior at stresses above 2 Pa, representing the effect of a higher amount of fibrillation and fiber entanglement by use of an additional interaction chamber of 200 μm. The decrease in creep compliance with number of passes also demonstrates the influence of amount of fibrillation on creep compliance and strain recovery of suspensions with a gel-like behavior.

- For the fourth group S7, S8, S9 (Fig. 9), the suspensions show viscoelastic behavior at 2 and 5 Pa or viscous behavior at 20 Pa. At low stress (Fig. 9a), a stepwise increment of 5, 10 and 15 number of passes within the 87 μm chamber results in a maximum creep compliance of 0.06, 0.04 and 0.05 Pa$^{-1}$, respectively. At high stress (Fig. 9b), the sample S8 shows lower creep compliance than sample S9 in parallel with the intermediate stress of 5 Pa (Fig. 9c), while the creep compliance of S8 and S9 is quite similar at lower stress of 2 Pa. In this concern, the increment of number of passes would not necessarily produce MFC/NFC suspensions with linear rheological properties. However, the gel-like behavior of all samples was observed at low stresses, in parallel with oscillatory data below.

The creep compliance $J_c(t)$ results from the ratio of strain ($\gamma$) to stress ($\tau$) and represents the deformation per unit stress in time. The viscoelasticity of MFC/NFC suspension was characterized by the Burger model, based on the creep data at stress of 2 Pa for samples from the second, third and fourth group. The Burger model (see supplementary information SI5) with a serial combination of the Maxwell and Kelvin–Voigt units can be used for a phenomenological description of the creep compliance $J_c(t)$ under steady-state conditions, as a function of time by the following Eq. (5) (Barnes 2000):

$$J_C(t) = \frac{1}{G_0} + \frac{1}{G_1}\left[1 - exp\left(\frac{-tG_1}{\eta_1}\right)\right] + \frac{t}{\eta_0} \qquad (5)$$

where ($G_0$) is the instantaneous elastic modulus of the Maxwell unit, ($G_1$) is the elastic modulus of the Kelvin–Voigt unit, ($\eta_0$) is the residual viscosity of the dashpot in the Maxwell and ($\eta_1$) represents internal viscosity of the dashpot in the Kelvin–Voigt element (Barry 1983).

The parameters ($G_0$, $G_1$, $\eta_0$, $\eta_1$) allow to compare the internal structure of the MFC/NFC suspensions in response to the deformation in a first approximation under steady-state creep conditions, as shown by the fitting curves in Fig. 10a. According to the calculated values in Table 4, the elastic moduli $G_0$ and $G_1$ are most predominant at stress of 2 Pa. The values $G_1 > G_0$ for different sample groups (S2, S5 and S8) can be explained by the flexibility of each system before deformation. Moreover, $\eta_0 > \eta_1$ indicates that
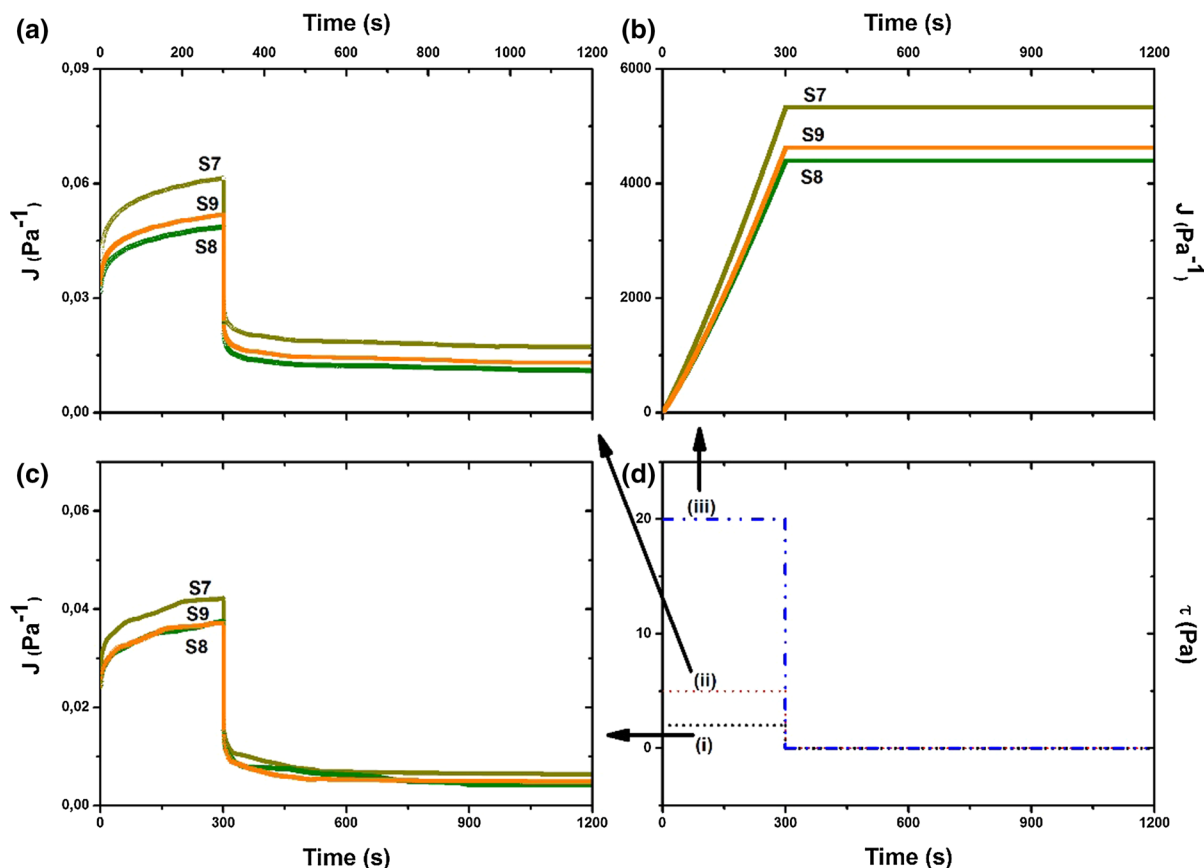
**Fig. 9** Creep and strain recovery test of MFC/NFC suspensions (0.5 wt%) processed within homogenizer and 200 μm chambers; **a** creep and strain recovery compliance versus time at stress 5 Pa, **b** creep and strain recovery compliance versus time at stress 20 Pa, **c** creep and strain recovery compliance versus time at stress 2 Pa, **d** stress versus time. Tests were done for $t_{Creep} = 300$ s and strain recovery (zero stress) for $t_{Recovery} = 900$ s at 25 °C

the instantaneous deformation is larger than the creep deformation at a stress of 2 Pa. For all MFC/NFC suspensions, the contribution of the Maxwell spring (i.e., permanent deformation) is larger than the contribution of the Kelvin–Voigt element (i.e., time-dependent deformation) relatively to the total deformation. As mentioned before, the sample from the fourth group (S8) has a higher amount of fibrillation than samples from the third and second group (S5 and S2), however by taking into account the fitting parameters, it can be concluded that the fiber network of sample S5 is more stable than for sample S8. The strain recovery plots for different samples per group (S2, S5 and S8) show first an instantaneous recovery and then a step-like recovery, as shown in Fig. 10b: the instantaneous recovery occurs irrespectively of the chamber size and number of passes, but the sample S8

that was processed in the smallest chamber shows up to four steps in strain recovery, which might occur by progressive relaxation of the strongly entangled fiber network.

Oscillatory rheology

The rheological properties in oscillatory testing of optimum processed MFC/NFC suspensions (H2, S2, S5 and S8) were studied in a strain sweep (Fig. 11a) and frequency sweep (Fig. 11b) test.

The strain sweep plots (Fig. 11a) show a linear regime with a Newtonian plateau at low strain up to 0.1 %. The lower values of loss modulus compared to storage modulus ($G'' < G'$) indicate that the gel-like properties dominate at low strain. With increment of strain, the loss and storage modulus of samples S2, S5
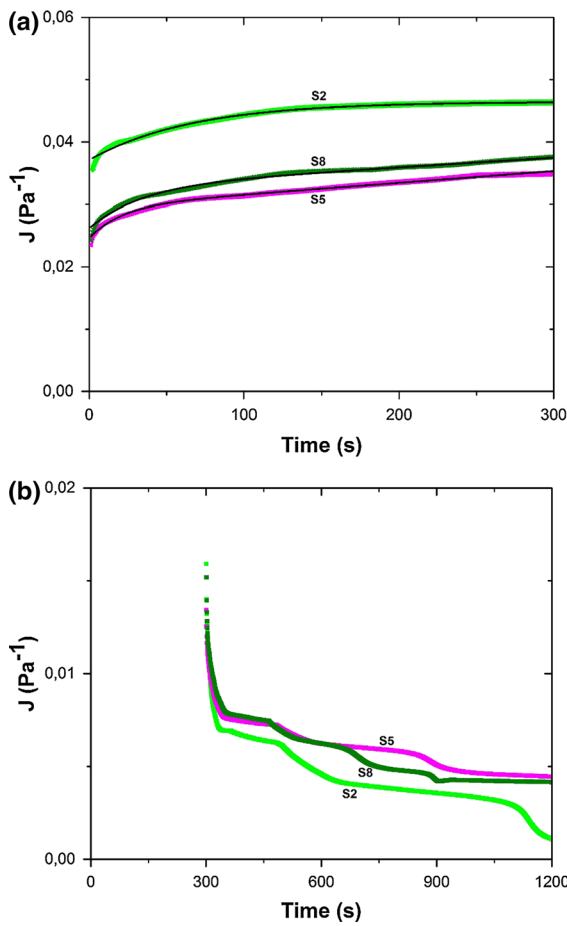
Fig. 10 a Burger's model fits of creep data for MFC/NFC suspensions (0.5 wt%), b strain recovery comparison of MFC/NFC suspensions (0.5 wt%). The stress of 2 Pa for $t_{Creep} = 300$ s was applied and after unloading the strain recovery for $t_{Recovery} = 900$ s at 25 °C is plotted



Fig. 11 Oscillation rheometry for different groups of MFC/NFC suspension (0.5 wt%) at 25 °C; a strain sweep test, b frequency sweep test. The *solid symbols* represent storage modulus ($G'$) and the *open symbols* represent loss modulus ($G''$)

and S8 start to change at 0.1 % strain and the cross-over of $G''$ and $G'$ was observed at 0.3 % strain, indicating the transition into liquid behavior. This behavior represents a strain dependency of the elastic modulus and "softening" under higher deformation
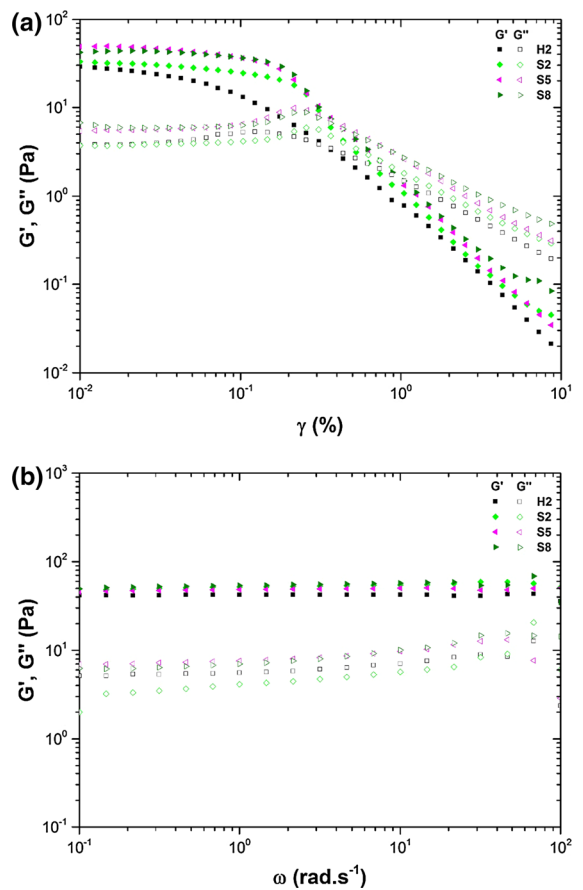
characterized by a decrement of the modulus. The limitation of the linear regime for MFC/NFC suspensions correlates with a dynamic yield point that occurs at almost the same strain of 0.2 % for samples S2, S5, S8. The smooth increment of loss modulus ($G''$) close to the cross-over point represents the dynamic yield point. The cross-over point can be related to yield

Table 4 Creep parameters according to the Burger's model fitted by Eq. (5) under stress of 2 Pa

| Parameters | Samples | | |
|---|---|---|---|
| | S2 | S5 | S8 |
| $G_0$ (Pa) | $28.82 \pm 0.01$ | $40.63 \pm 0.01$ | $38.18 \pm 0.01$ |
| $G_1$ (Pa) | $152.67 \pm 0.01$ | $198.41 \pm 0.01$ | $151.05 \pm 0.01$ |
| $\eta_0 \times 10^{-4}$ (Pa s) | $8.00 \pm 0.54$ | $5.29 \pm 0.03$ | $6.45 \pm 0.11$ |
| $\eta_1 \times 10^4$ (Pa s) | $1.44 \pm 0.08$ | $2.43 \pm 0.06$ | $1.95 \pm 0.05$ |
| $r^2$ | 0.98 | 0.99 | 0.99 |

stress: in more detail, a higher number of passes or smaller chamber increases the yield stress of the MFC/NFC suspensions, as also concluded from Fig. 6b. Unlikely, the onset of strain thinning for sample H2 occurred at a strain below 0.3 % and the maximum in loss modulus was less intense, while the cross-over point was observed at somewhat higher strain. In conclusion, the increment of strain directly influences viscoelastic properties of MFC/NFC suspensions due to breakage of networks and the elastic-to-viscous transition shows that viscous losses dominate over elasticity beyond the cross-over point. However, the gel-like properties for inhomogeneous samples with less fibrillation are less clear.

The frequency sweep plots (Fig. 11b) show almost a linear behavior of storage modulus and slow increment of loss modulus with increasing of frequency, where fiber entanglements might gain more importance. The values $G'' < G'$ confirm the gel-like behavior over the entire frequency range. The storage moduli $G'$ of samples that were processed with more than one chamber (homogenizer, 200 and 87 μm) are close and independent of frequency. In comparison, the mean values of loss and storage moduli at a specific frequency and strain are in agreement with previous strain sweep measurements ($\omega = 0.6$ rad s$^{-1}$ and $\gamma = 0.05$ %).

## Conclusion

The effects of processing parameters in a microfluidizer (i.e., size of interaction chamber and the number of passes) have been related to morphology (SEM, TEM and AFM), physicochemical analysis (Zeta potential, WAXD and FTIR) and rheological data of micro- and nanofibrillated cellulose (MFC/NFC).

The smallest fiber diameters (45 to 15 nm) were limited by the chamber size and the largest fiber diameters further reduced (25 μm to 50 nm) with number of passes, thereby improving the homogeneity in fiber morphology. An optimum number of passes and chamber size was characterized by most negative zeta potential (-48.8 to -67.0 mV), resulting in a good balance between amount of fibrillation and stability of the suspension. The use of a smaller interaction chamber resulted in lower fiber crystallinity while a higher in number of passes slightly increased the fiber crystallinity, which might be related to the formation of an oriented nematic phase.

The rheometry data strongly fluctuated for samples processed within a homogenizer chamber due to flocculation of thin and thick fibers. For the optimum processed samples, the viscosity increased with higher amount of fibrillation by using a smaller chamber or higher number of passes, and a Newtonian plateau occurred at intermediate shear rates of 2–40 s$^{-1}$ due to temporary aggregation and breaking-up of the fiber network. With a too high number of the passes, however, the viscosity dropped because of aggregation of fine fibers. This can also be related to the aspect ratio variations during processing which decreases the percolation threshold. In parallel, a higher number of passes leads to lower creep compliance and a step-like strain recovery, which represents the progressive relaxation of an entangled fiber network. From dynamic rheometry, the gel-like properties are dominating at low strain while a dynamic yield point occurs at almost the same strain of 0.2 % for samples: the behavior is less clear for poorly homogenized samples, while it is almost independent of processing conditions for optimized samples. The calculation of yield stress from Herschel–Bulkley fits showed that chamber size has a more important effect on the yield stress than number of passes. The total number of passes applied in processing of MFC/NFC suspensions can be directly related to rheological and morphological data by introducing the rotational Péclet number. Based on this value, the processing parameters can be adapted towards specifically required rheological properties.

## References

Abdul Khalil APS, Bhat AH, Ireana Yusra AF (2012) Green composites from sustainable cellulose nanofibrils: a review. Carbohydr Polym 87:963–979

Adebajo MO, Frost RL (2004) Infrared and 13C MAS nuclear magnetic resonance spectroscopis study of acetylation of cotton. Spectrochim Acta A 60:449–453

Barnes HA (1999) The yield stress: a review or 'παντα ρει'—everything flows? J Non Newtonian Fluid Mech 81:133–178

1237

Barnes HA (2000) A handbook of elementary rheology. Institute of Non-Newtonian Fluid Mechanics Wales, University of Wales, Aberystwyth

Barry BW (1983) Rheology of dermatological vehicles. Marcel Dekker, New York

Benhamoua K, Dufresne A, Magninc A, Mortha G, Kaddami H (2013) Control of size and viscoelastic properties of nanofibrillated cellulose from palm tree by varying the TEMPO-mediated oxidation time. Carbohydr Polym 99:74–83

Björkman U (2003) Break-up of suspended fibre networks. Nord Pulp Pap Res J 18:32–37

Bröckel U, Meier W, Wagner G (2013) Product design and engineering: formulation of gels and pastes. Wiley-VCH Verlag, Heidelberg

Charani PR, Firouzabadi MD, Afra E, Shakeri A (2013) Rheological characterization of high concentrated MFC gel from kenaf unbleached pulp. Cellulose 20:727–740

Chen P, Yu H, Liu Y, Chen W, Wang X, Ouyang M (2013) Concentration effects on the isolation and dynamic rheological behavior of cellulose nanofibers via ultrasonic processing. Cellulose 20:149–157

Derakhshandeh B, Hatzikiriakos SG, Bennington CPJ (2010) The apparent yield stress of pulp fiber suspensions. J Rheol 54:1137–1154

Dinand E, Chanzy H, Vignon M (1996) Parenchymal cell cellulose from sugar beet pulp: preparation and properties. Cellulose 3:183–188

French AD (2014) Idealized powder diffraction patterns for cellulose polymorphs. Cellulose 21:885–896

Henn AR, Fraundorf PB (1990) A quantitative measure of the degree of fibrillation of short reinforcing fibres. J Mater Sci 25:659–3663

Herrick FW, Casebier RL, Hamilton JK, Sandberg KR (1983) Microfibrillated cellulose: morphology and accessibility. J Appl Polym Sci Appl Polym Symp 37:797–813

Hill RJ (2008) Elastic modulus of microfibrillar cellulose gels. Biomacromolecules 9:2963–2966

Hubbe MA (2007) Flocculation and redispersion of cellulosic fiber suspension: a review of effects of hydrodynamic shear and polyelectrolyte. Bioresources 2:296–331

Iotti M, Gregersen Ø, Moe S, Lenes M (2011) Rheological studies of microfibrillar cellulose water dispersions. J Polym Environ 19:137–145

Iwamoto S, Nakagaito AN, Yano H (2007) Nano-fibrillation of pulp fibers for the processing of transparent nanocomposites. Appl Phys A Mater Sci Process 89:461–466

Iwamoto S, Abe K, Yano H (2008) The effect of hemicelluloses on wood pulp nanofibrillation and nanofiber network characteristics. Biomacromolecules 9:1022–1026

Janardhnan S, Sain M (2011) Targeted disruption of Hydroxyl chemistry and crystallinity in natural fibers for the isolation of cellulose nano-fibers via enzymatic treatment. Bioresources 6:1242–1245

Kacuralova M, Capek P, Sasinklova V, Wellner N, Ebringerova A (2000) FT-IR study of plant cell wall model compounds: pectic polysaccharides and hemicelluloses. Carbohydr Polym 43:195–203

Karande VS, Bharimalla AK, Hadge GB, Mhaske ST, Vigneshwaran N (2011) Nanofibrillation of cotton fibers by

disc refiner and its characterization. Fibers Polym 12:399–404

Karppinen A, Vesterinen AH, Saarinen T, Pietikäinen P, Seppälä J (2011) Effect of cationic polymethacrylates on the rheology and flocculation of microfibrillated cellulose. Cellulose 18:1381–1390

Karppinen A, Saarinen T, Salmela J, Laukkanen A, Nuopponen M, Seppälä J (2012) Flocculation of microfibrillated cellulose in shear flow. Cellulose 19:1807–1819

Kataoka Y, Kondo T (1998) FTIR microscopic analysis of changing cellulose crystalline structure during wood cell wall formation. Macromolec 31:760–764

Kondo T (1997) The assignment of IR absorption bands due to free hydroxyl groups in cellulose. Cellulose 4:281–292

Kondo T, Togawa E, Brown RM (2001) Nematic ordered cellulose: a concept of glucan chain association. Biomacromolecules 2:1324–1330

Lasseuguette E, Roux D, Nishiyama Y (2008) Rheological properties of microfibrillar suspension of TEMPO-oxidized pulp. Cellulose 15:425–433

Li MC, Wu Q, Song K, Lee S, Qing Y, Wu Y (2015) Cellulose nanoparticles: structure–morphology–rheology relationships. ACS Sustainable Chem. Eng 3:821–832

Lowys MP, Desbrières J, Rinaudo M (2001) Rheological characterization of cellulosic microfibril suspensions. Role of polymeric additives. Food Hydrocoll 15:25–32

Masalova I, Malkin AY, Foudazi R (2008) Yield stress of emulsions and suspensions as measured in steady shearing and in oscillations. Appl Rheol 18:44790–1–44790-8

Mewis J, Wagner NJ (2009) Current trends in suspension rheology. J Non Newton Fluid Mech 157:147–150

Missoum K, Belgacem N, Krouit M, Martin C, Tapin-Lingua S, Bras J (2010) Influence of fibrillation degree and surface grafting of microfibrillated cellulose on their rheological behavior in aqueous suspension. In: TAPPI Nanotechnology conference for the forest product industry

Moon RJ, Martini A, Nairn J, Simonsen J, Youngblood J (2011) Cellulose nanomaterials review: structure, properties and nanocomposites. Chem Soc Rev 40:3941–3994

Nechyporchuk O, Belgacem MN, Pignon F (2014) Rheological properties of micro-/nanofibrillated cellulose suspensions: wall-slip and shear banding phenomena. Carbohydr Polym 112:432–439

Nelson ML, O'Connor RL (1964) Relation of certain infrared bands to cellulose crystallinity and crystal latticed type. Part I. Spectra of lattice types I, II, III and of amorphous cellulose. J Appl Polym Sci 8:1311–1324

Oh SY, Yoo DI, Shin Y, Seo G (2005) FTIR analysis of cellulose treated with sodium hydroxide and carbon dioxide. Carbohydr Res 340:417–428

Ono H, Shimaya Y, Sato K, Hongo T (2004) 1H spin–spin relaxation time of water and rheological properties of cellulose nanofiber dispersion, transparent cellulose hydrogel (TCG). Polym J 36:684–694

Pääkkö M, Ankerfors M, Kosonen H, Nykänen A, Ahola S, Österberg M, Ruokolainen J, Laine J, Larsson PT, Ikkala O, Lindström T (2007) Enzymatic hydrolysis combined with mechanical shearing and high-pressure homogenization for nanoscale cellulose fibrils and strong gels. Biomacromolecules 8:1934–1941

Saarikoski E, Saarinen T, Salmela J, Seppälä J (2012) Flocculated flow of microfibrillated cellulose water suspensions: an imaging approach for characterisation of rheological behavior. Cellulose 19(3):647–659

Saito T, Nishiyama Y, Putaux J, Vignon M, Isogai A (2006) Homogeneous suspensions of individualized microfibrils from TEMPO-catalyzed oxidation of native cellulose. Biomacromolecules 7:1687–1691

Salmén L, Åkertholm M, Hinterstoisser B (2005) Polyssaccharides: structural diversity and functional versatility. New York, USA

Segal L, Creely JJ, Martin AE Jr, Conrad CM (1959) An empirical method for estimating the degree of crystallinity of native cellulose using the X-ray diffractometer. Text Res J 29:786–794

Shogrena RL, Peterson SC, Evans KO, Kenar JA (2011) Preparation and characterization of cellulose gels from corn cobs. Carbohydr Polym 86:1351–1357

Taheri H, Samyn P (2015) Rheological properties and processing of polymer blends with micro- and nanofibrillated cellulose. In: Hakeem KR, Jawaid M, Alothman OY (eds) Agricultural biomass based potential materials. Springer, Switzerland, pp 259–291

Tatsumi D, Ishioka S, Matsumoto T (2002) Effect of fiber concentration and axial ratio on the rheological properties of cellulose fiber suspensions. J Soc Rheol Jpn 30:27–32